remote sensing

MDPI

Article

Design of Scanning Units for the Underwater Circumferential-Scanning LiDAR Based on Pyramidal-Shaped Reflectors and a Rapid Detection Method for Target Orientation

Bingting Zha [1,2,*,†], Guangbo Xu [1,†], Zhuo Chen [1], Yayun Tan [3], Jianxin Qin [1] and He Zhang [1]

[1] Ministerial Key Laboratory of ZNDY, Nanjing University of Science and Technology, Nanjing 210094, China; xgbxgb@njust.edu.cn (G.X.); chenz@njust.edu.cn (Z.C.); qinjianxin@njust.edu.cn (J.Q.); hezhangz@njust.edu.cn (H.Z.)
[2] Science and Technology on Electromechanical Dynamic Control Laboratory, Beijing 100081, China
[3] Navy Department, No. 28th Research Institute of China Electronics Technology Group Corporation, Nanjing 210094, China; tyy15380833755@163.com
* Correspondence: zhabingting@njust.edu.cn
† These authors contributed equally to this work.

Abstract: Challenges have been observed in the traditional circumferential-scanning LiDAR underwater to balance between the detection range and the sealing performance. To tackle these challenges, a new scanning unit is presented in this paper, employing a pyramidal-shaped reflector for enhanced performance. Furthermore, an innovative magneto–electric detection module comprising Hall switches and magnetic rings is introduced. It can facilitate the accurate identification of the reflector's edge, thereby enhancing the precision of the target-orientation detection. A rapid target orientation coding method based on split-frequency clocks is proposed on FPGAs. It can output the target's initial and termination orientation codes immediately after capturing it, exhibiting a significantly low output delay of 20 ns and a high detection resolution of 15°. Finally, a prototype is fabricated to validate the design in this paper. The experimental results demonstrate that the scanning unit enables reliable scanning and orientation recognition of the target. In addition, it is trustworthy in receiving echo signals when the laser passes through glass and then an aqueous medium.

Keywords: LiDAR; pyramidal reflector; multi-parameter optimization; orientation identification

Citation: Zha, B.; Xu, G.; Chen, Z.; Tan, Y.; Qin, J.; Zhang, H. Design of Scanning Units for the Underwater Circumferential-Scanning LiDAR Based on Pyramidal-Shaped Reflectors and a Rapid Detection Method for Target Orientation. *Remote Sens.* **2024**, *16*, 2131. https://doi.org/10.3390/rs16122131

Academic Editor: Nicolas Baghdadi

Received: 7 April 2024
Revised: 2 June 2024
Accepted: 10 June 2024
Published: 12 June 2024

1. Introduction

Autonomous Underwater Vehicles (AUVs) are becoming increasingly intelligent and represent the future trend in maritime equipment. They can operate in highly dangerous sea areas, and extend the scope of underwater combat. Laser radar (LiDAR) is an essential technology for AUVs to achieve undersea terrain mapping, mine reconnaissance, underwater target identification, and localization [1–10].

Many researchers have worked on underwater LiDAR. In the late 20th century, Westinghouse developed the SM2000 underwater scanning imaging LiDAR, which utilizes a solid-state blue-green laser and a rotating scanning mirror to direct a laser beam onto a narrow area of the seafloor. It has a maximum scanning angle of 70° and a minimum scanning angle of 15° [11]. LUCIE (Laser Underwater Camera Image Enhancer), developed in Canada, is used for underwater UUVs and handheld applications. It uses a 532 nm laser of 2 kHz frequency and 80 mW average power as an illumination source, received by a 10 cm diameter zoom lens. In areas with clear water, a target of 7 m can be obtained [12]. Karman Corporation of the United States has developed the famous "Magic Lantern" series of airborne laser imaging systems to detect mines on and below the water's surface. The system uses a line scanning blue-green laser and selective image enhancement camera PG-LLS imaging mode on the sea surface 120~460 m above the altitude of operation, with a detection depth of 12~61 m [13]. Teledyne Optech, Vaughan, Canada, has proposed an

underwater LiDAR called CZMIL. It uses a new 10 kHz green light pulsed laser as a light source and a 20 cm rotating Fresnel scanning mirror as a scanner. The CZMIL scanner can detect targets from 0 to 30 m underwater [14]. In 2015, Huazhong University of Science and Technology (HUST) designed a compact pulsed LiDAR system utilizing a 12-ns doubled-frequency pulsed Nd: YAG laser. The system features a single-pulse energy of 4 mJ and incorporates a transmitting optics system comprising a transmitting collimating lens and beam splitter. It is capable of acquiring targets within a range of 20 m underwater with an attenuation coefficient of 0.67 m^{-1} [15]. Heriot-Watt University (UK) has pioneered the initial implementation of photon-counting LiDAR for underwater target detection. It involves exploring a depth-imaging system designed for high-scattering underwater environments, utilizing time-of-flight and time-correlated single-photon counting (TCSPC). The system consists of a pulsed supercontinuum laser source, a static scanning manipulator, and a silicon single photon avalanche diode (SPAD) for detecting the returning optical signals, which can realize depth imaging of close-range targets without scanning function [16].

Most scholars in these studies are dedicated to enhancing underwater laser detection's accuracy and detection range. Nevertheless, this often results in an increase in the size and complexity of underwater LiDAR systems. In addition, there are fewer studies on circumferential-scanning LiDAR in the existing research, while underwater target detection or imaging is not limited to seabed or fixed targets. When the underwater LiDAR faces moving targets, circumferential scanning capability is required.

Circumferential-scanning underwater LiDAR should be able to detect the distance and direction of any target around the entire circumference [17–25]. To realize it, the four-quadrant transceiver scheme has been widely used in air conditions. This is due to the fact that laser emission in air typically involves the use of beam expanding lasers, which utilize a specific optical system to expand the laser's spot into a rectangle with a 90° angle. However, for underwater LiDAR, expanding the laser spot can severely shorten the detection range. Therefore, the traditional underwater LiDAR commonly employ a 360° completed-circumferential scanning detection system with a single beam, primarily attributable to limitations in laser energy and considerations for heat dissipation [17–25].

The single-beam sync-scanning LiDAR necessitates a substantial ring of light-transmitting glass reinforced with stiffeners to enhance load-bearing capacity [26]. This configuration will introduce a fan-shaped scanning blind spot, significantly constraining the LiDAR's capability to capture high-speed moving targets [27]. In terms of sealing performance, the ring-shaped light-transmitting glass poses difficulties in ensuring a snug fit against the end face. So, it is not suitable for effective sealing using an O-ring. Hence, traditional scanning methods are impractical in environments that require stringent sealing performance, such as underwater or densely smoke-laden conditions.

Since it is difficult to balance between the detection range and the sealing performance, the underwater LiDAR cannot adopt a four-quadrant transceiver scheme previously. To solve this problem, this paper proposes a new scanning unit based on a pyramidal-shaped reflector.

In orientation detection, the temporal interval between adjacent pulses is smaller when the laser frequency is high [27]. Thus, meeting the sampling frequency and data transmission rate requirements of orientation detection modules via serial communication poses a substantial challenge. The conventional approach involves employing a magnetic steel co-rotating with the motor, coupled with a magnetic sensor gauging the rotational period of the magnet [28]. Subsequently, the target's orientation is predicted based on the arrival moment of the laser echo signal. A limitation of this approach is that it delivers the target's orientation as a timing outcome, which requires the deployment of a complex solver algorithm to convert this timing result into an angular measurement. Thus, it cannot employ more intricate algorithms for real-time processing.

Furthermore, conventional methods have limitations in accurately distinguishing the precise edge of the pyramidal reflector where the target is located. There is a risk of making a significant error in determining the target's orientation. Therefore, this paper proposed a

novel magneto–electric detection module comprising Hall switches and magnetic rings to achieve nanosecond-level recognition of the reflector's edges.

Given large-volume targets, novel detection strategies have been devised for targeting their reasonable areas. Additionally, this paper presents a real-time correction method for motor speed based on finite-state machines via the parallel processing capability on FPGAs [29]. A rapid target orientation coding method for target orientation was designed via split-frequency clocks. It achieves the "single-chip" signal processing for the scanning unit and significantly enhances the speed of target orientation detection. The prototype test results indicate that the proposed design in this study effectively fulfills the detection requirements of underwater LiDARs.

2. Design and Optimization of Scanning Unit Based on the Pyramidal-Shaped Reflector

2.1. Design of the Scanning Unit

Traditional underwater LiDARs typically employ a detection method by a single-beam, as illustrated in Figure 1. It involves the initiation of a pulsed laser beam from the laser positioned at the center of the LiDAR towards the scanning mechanism. The scanning mechanism drives the reflector to rotate by 360°, thereby generating a scanning trajectory of the laser [24]. The researchers took this approach for the following main reasons:

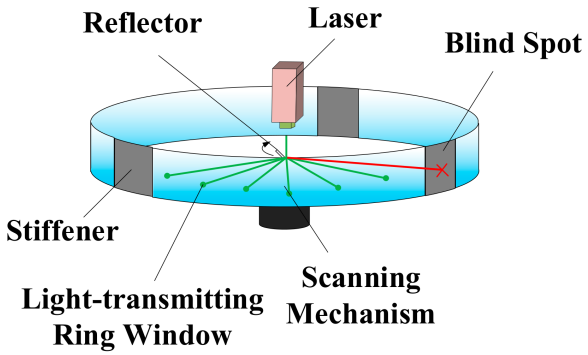

Figure 1. The detection method by a single-beam.

(1) To achieve a detection distance of about 10 m, the peak power of the pulsed laser often has to be greater than 20 kW. To accomplish this, we need to make the spot of the laser emission as small as possible. Therefore, the researchers use a scanning mechanism to cover the entire circumference.

(2) After that, the researchers need a light-transmitting ring window to transmit the laser output from the scanning mechanism to the water. However, the ring window's sealing performance is poor.

As elucidated in the introduction, the single-beam detection method has shortcomings related to suboptimal sealing performance, fan-shaped blind spots, and limited resistance to interference. In summary, a way to balance the detection range and sealing performance is to use a small laser spot and a scanning mechanism but to avoid ring windows.

The researcher had proposed a four-quadrant pulsed laser transceiver scheme [27], as illustrated in Figure 2a. The laser emission is partitioned into four-quadrants. To enhance the extraction of target information while preserving adequate laser emission power, the laser selectively emits from two opposite direction quadrants, such as ① and ③ simultaneously, followed by ② and ④ in an alternating fashion. This approach achieves a comprehensive 360° scanning of the LiDAR.

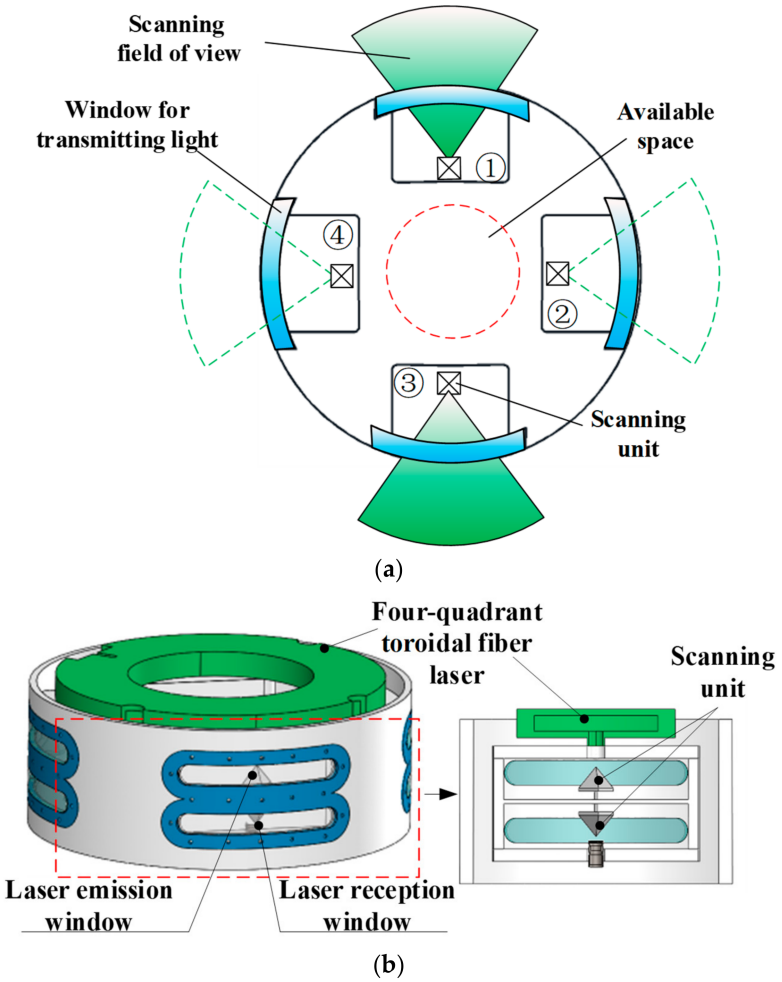

Figure 2. Schematic diagram of the four-quadrant pulse laser transceiver scheme: (**a**) Scanning scheme; (**b**) Scanning structure.

Building upon the aforementioned scanning scheme, this study introduced a scanning unit, employing a pyramidal-shaped reflector (hereinafter referred to as the reflector), allocated to each of the four quadrants illustrated in Figure 2b. In this manner, we achieve a small laser spot and a scanning mechanism, thereby avoiding the presence of ring windows.

The scanning unit comprises a pyramidal reflector, a brushless motor, a magneto–electric detection module (comprising a Hall switch and a magnetic ring), a receiving lens, and a receiving circuit. As depicted in Figure 3, the laser beam is directed from the top of the scanning unit. The brushless motor drives the reflector to perform rotational motion, enabling the laser to scan back and forth within the field of view, and then forms a scanning trajectory. The receiving circuit captures the return energy of the laser, enabling the extraction of target distance and orientation information.

The novel design of the underwater LiDAR divides the circumferential scanning field of view into four quadrants. Each quadrant is hermetically sealed using small light-transmitting windows and O-rings, thereby significantly enhancing the sealing performance of the LiDAR. The scanning field of view achieved by the four scanning units ensures comprehensive circumferential coverage of the scanning laser, effectively reducing the fan-shaped scanning blind spot typically associated with stiffener usage. Furthermore, incorporating four independent scanning units enhances the availability of target information for the LiDAR, thereby facilitating signal processing algorithms to achieve more functions.

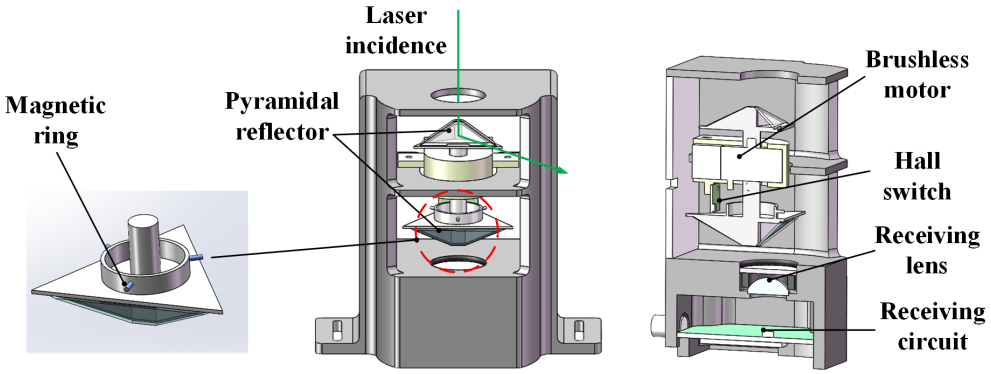

Figure 3. Schematic diagram of the scanning unit.

2.2. Multi-Parameter Optimization Design for Pyramidal Reflector

The operational principle of the pyramidal reflector is illustrated in the figure below. The laser emits a pulsed laser beam, denoted as P, which is directed along the axis of the reflector. The beam undergoes completed reflection within a specialized film, creating a scanning laser beam denoted as p'. The resulting beam, p', reaches the target plane and generates a series of scanning points.

Simultaneously, the brushless motor drives the reflector into continuous rotation at a speed denoted as n_d. Simultaneously, the variation in the scanning deflection angle φ directs the scanning laser beam, p', to different positions on the target plane, creating the scanning trajectory.

As depicted in Figure 4, n_p represents the normal direction to the pyramid surface of the reflector. h is the vertical distance between the pulsed laser beam P and the target plane. The straight-line distance from the reflection point O to the target plane is defined as the scanning radius, R. θ signifies the cone angle of the reflector surface relative to its base. According to trigonometric relations, θ is numerically equal to the angle between P and the normal n_p. The pulse frequency of P is denoted as f_p, and the angle α between two adjacent pulsed laser beams can be expressed as below:

$$\alpha = 2\pi n_d / f_p. \tag{1}$$

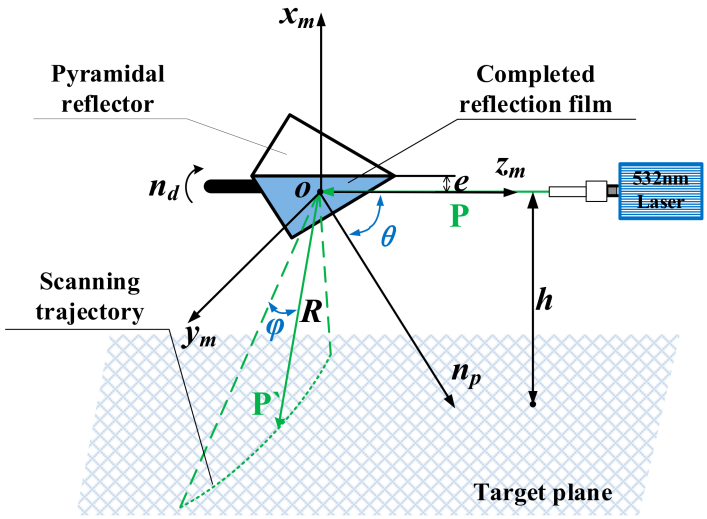

Figure 4. Laser scanning trajectory model diagram.

The directional perspective of the reflector is derived from the incident direction of the laser beam, as illustrated in Figure 5. The center of the reflector was O', and l represents the length of the reflector's side; e denotes the eccentricity of the pulsed laser beam P with respect to O'.

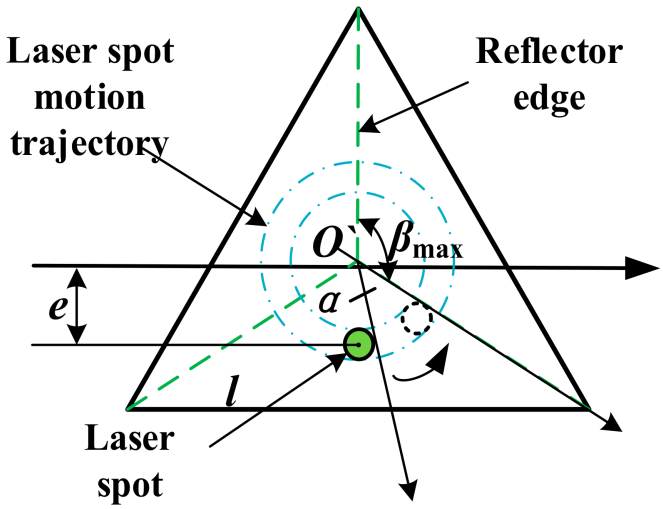

Figure 5. Reflector view of laser incident direction.

Utilizing the counter-rotating method, the reflector remains stationary, thereby yielding the motion trajectory of the laser spot depicted in the Figure 5. The quantity of edge in the reflector is denoted as k, whereby the maximum field of view $\beta_{\max}$ of the scanning unit is determined as $2\pi/k$.

As the laser spot reaches the periphery of the reflector, its laser reflectivity undergoes a sudden change. It results in a temporary void in scanning trajectory until the laser spot relocates entirely to the adjacent edge of the reflector.

Hence, the theoretical field angle β of the scanning unit is expressed as follows:

$$\beta = \beta_{\max} - 2\alpha. \tag{2}$$

The following considerations were made to enhance the reliability of the scanning process, which ensures that the laser spot is positioned at the center of the projection on the surface of the reflector,

$$e = \frac{l}{4 \cdot \tan(\pi/k)} \tag{3}$$

The scanning unit is designed with a minimum scanning frequency that does not miss the targets, as elaborated in the reference [23]. This can be expressed mathematically as below:

$$f_{s\ \min} = \frac{v_t + v_m}{L_t} \tag{4}$$

where v_t denotes the target velocity, v_m represents the own velocity, and L_t signifies the target width. Consider the standard case where v_t = 55 KN, v_m = 45 KN, and L_t = 5.58 m, $f_{s\ \min} = 553.2$ r/min. However, increasing the scanning frequency alone may lead to only marginal improvements in target identification capability. This is because the target's relative position undergoes minimal change between successive scans, leading to limited variations in the echo signal.

The final scanning speed is mainly related to the motion speed of the typical target. To increase the probability of target capture, the underwater LiDAR is usually required to complete three scans in the time it takes to make a head-on encounter with the target. At this time, if the scanning speed is further increased, the target echo signal does not change much in the adjacent pulse time. However, the power consumption, noise, and

electromagnetic interference is generated by the brushless motors with increased scanning speed. Consequently, the motor speed (scanning speed) n_{d} is determined by the following equation:

$$n_d = \frac{3 \times f_{s\ \min}}{k}. \tag{5}$$

As depicted in Figure 2, this study employed four scanning units to achieve a comprehensive 360° scanning. Consequently, each scanning unit requires a field-of-view angle (β) of at least 90°, and the number of prismatic edges (k) of the reflector in this paper is stipulated as 3.

The correlation between the theoretical field of the view angle (β) and the pulse frequency (f_{p}) is graphically depicted in Figure 6, which is derived from Equation (5) when n_{d} = 553.2 r/min. Below the preferred line, the slope of the theoretical field-of-view angle (β) is steeper, resulting in substantial fluctuations in the field of the view even with minor adjustments in pulse frequency. It may cause the view angle to drop below 90°, which is unfavorable for maintaining the stability of laser scanning.

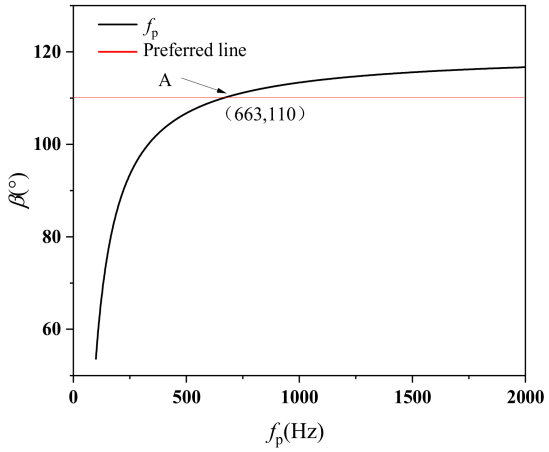

Figure 6. The relationship between the theoretical field angle β and the pulse frequency f_{p}.

Therefore, in order to reduce the fluctuation in the theoretical field of the view angle (β), it is essential for the pulse frequency (f_{p}) to exceed a minimum threshold of 663 Hz.

Utilizing the Equations (1)–(5), the scanning deflection angle (φ) of the scanning beam P' evolves with the rotation motor as below:

$$\varphi = \mathrm{mod}[(m \cdot \alpha), \beta_{\max}] + \varphi_0 \tag{6}$$

where $\mathrm{mod}[A, B]$ stands for the remainder of A over B; $m = 1, 2, \ldots, \lfloor t \cdot f_p \rfloor$; $\lfloor \cdot \rfloor$ signifies the downward rounding process, and φ_0 denotes the initial angle of the scanning beam.

It is established that $\varphi = 0°$, where the projection of the scanning beam p' (as depicted in Figure 4) in the $Ox_{\mathrm{m}}y_{\mathrm{m}}$ plane aligns with the negative half-axis of the x_{m}-axis. Then, $\varphi \in (-\beta/2, \beta/2)$. Assuming $\varphi_0 = -\beta/2°$ and f_{p} = 1000 Hz, the subsequent figure illustrates the evolution of the deflection angle φ as the motor completes one rotation cycle.

As illustrated in Figure 7, when the motor completes one rotation cycle, it enables the execution of three scanning cycles. Each cycle corresponds to one of the three edges of the reflector. Along each edge, the deflection angle of the scanning beam transitions from the minimum value to the maximum value during the motor's rotation. Subsequently, the process repeats as the scanning beam switches to the next edge, constituting a recurring cycle. Consequently, the scanning unit employing a pyramidal reflector demonstrates a threefold increase in scanning efficiency compared to traditional single-beam sync-scanning solutions.

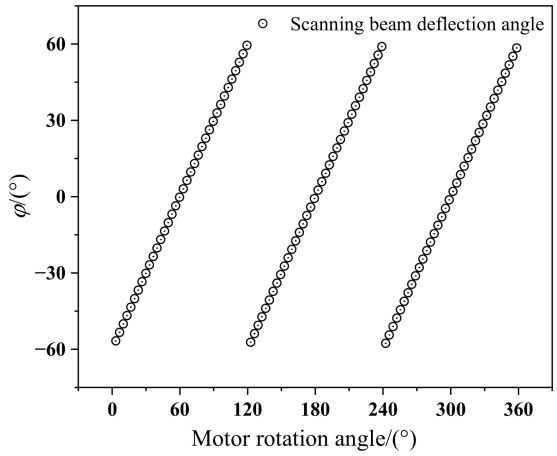

Figure 7. Change rules of motor scanning deflection angle φ.

As depicted in Figure 4, the definition of the reflection point O of the pulsed laser beam P is as the origin. The vertical direction is designated as the x-axis, and the ray passing through point O with an eccentric distance e from the reflector's axis represents the z-axis. By the principles of geometric optics, the laser scanning trajectory follows spherical coordinates:

$$\begin{cases} x_m = R \times \sin(2\theta) \times \cos(\pi - \varphi) \\ y_m = R \times \sin(2\theta) \times \sin(\pi - \varphi) \\ z_m = R \times \cos(2\theta) \end{cases} \tag{7}$$

In consideration of the geometric relationship illustrated in Figure 4, the formulation for R in Equation (7) is as follows:

$$R = \begin{cases} \frac{h}{\cos(2\theta) \cdot \cos\varphi}, & \theta \neq 45^\circ \\ \frac{h}{\cos\varphi}, & \theta = 45^\circ \end{cases} \tag{8}$$

where, θ represents an inherent characteristic of the reflector, and its value remains constant once the reflector's shape is established. Assuming $\theta = 60^\circ$, $h = 10$ m, and $t = 1$ s, the distribution of laser scanning trajectory and scanning point is as follows:

As depicted in Figure 8a, the laser scanning trajectory exhibits a parabolic shape on the target plane when $\theta = 60^\circ$. The scanning points demonstrate a higher density in proximity and a sparser distribution in the distal regions.

As depicted in Figure 8b, the temporal span when $t = 1$ s encompasses 1000 scanning points. Most of these points are concentrated within this interval ($z_m = [-7, -5.5]$), which accounts for more than half of the entire distribution. Nevertheless, within most of the remaining intervals ($z_m = [-12, -7]$), the density of scanning point distributions is notably low, which potentially leads to the overlooking of targets in these specific regions. Hence, in this scenario, the actual view field of the scanning unit is considerably smaller than the theoretical field.

Under unchanged conditions, the parameter θ is adjusted to 45° to achieve the laser scanning trajectory depicted in Figure 9. Observing that all the 1000 scanning points within the time frame ($t = 1$ s) are concentrated when $z_m = 0$, there is an absence of the parabolic shape, which is evident in Figure 8a. So, when $\theta = 45^\circ$, the z_m-axis coordinates of the scanning point remain constant with variations in the scanning deflection angle φ. To improve the reliability of the scanning unit and ensure a sufficiently large field of view angle, the cone angle of the reflector (θ) between the reflector surface and its bottom surface should be set to 45°.

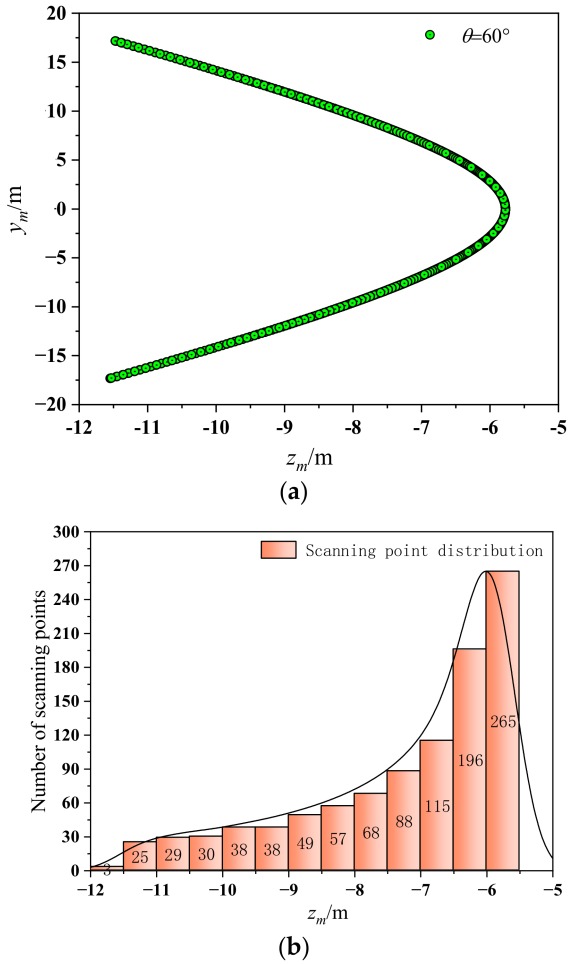

Figure 8. Laser scanning trajectory and scanning point distribution of θ = 60 °: (**a**) θ = 60° laser scanning trajectory; (**b**) Distribution of θ = 60° laser scanning points.

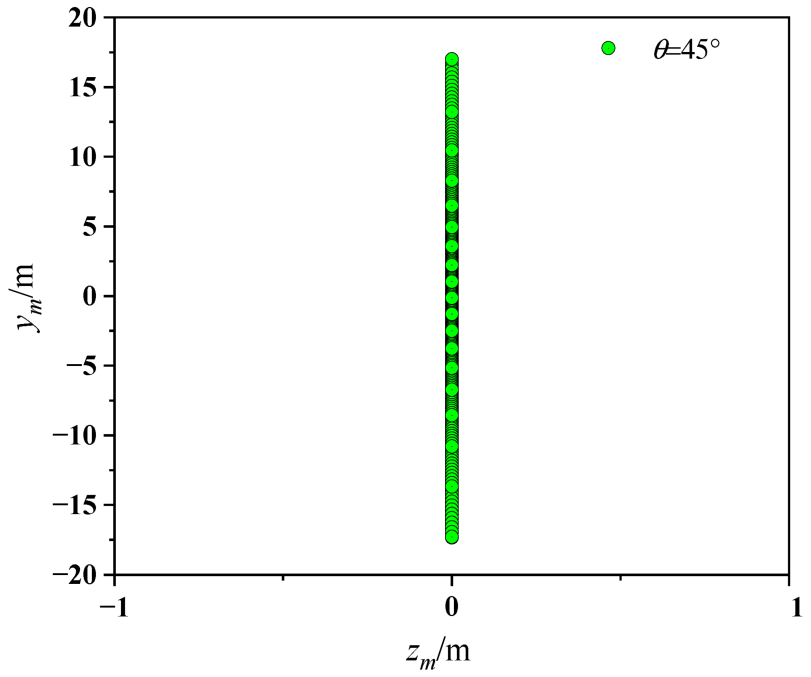

Figure 9. Laser scanning trajectory when θ = 45 °.

Based on the optimization results and the practical considerations in spatial arrangement, the design parameters for the pyramidal reflector are summarized in the following Table 1:

Table 1. Reflector's design parameters.

Parameter	Numerical Value
k	3
n_d	553.2 r/min
f_p	1000 Hz
α	3.3°
β	113.4°
θ	45°
l	15 mm
e	2.1 mm
h	10 mm

3. FPGA-Based Fast Detection Method for Target Orientation

3.1. Principles for Target Orientation Detection and Design of the Magneto-Electric Detection Modules

The traditional orientation detection method utilizing an optical-magnetic composite is illustrated in Figure 10a. A magnetic steel rotating in sync with the motor is attached to the spindle, and a Hall switch is alongside. During the rotational movement of the magnetic steel, the Hall switch generates a rising signal every time the pole aligns with the Hall switch, as shown in Figure 10b. The two adjacent Hall switch signals correspond to one rotation cycle of the motor.

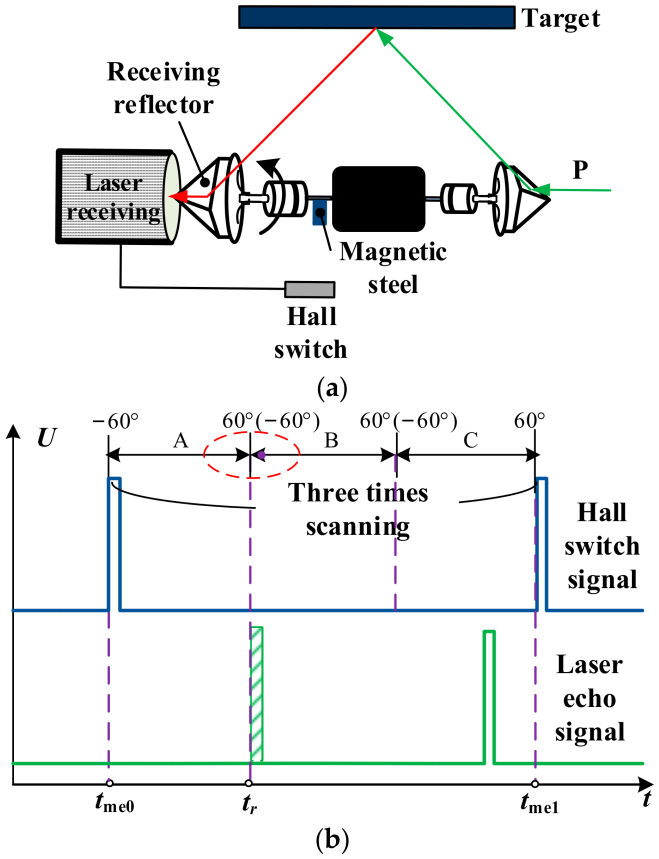

Figure 10. Traditional optical-magnetic composite orientation detection method and schematic of optical-magnetic composite signal: (**a**) Conventional orientation detection methods; (**b**) Optical-magnetic composite signal diagram.

The basic principle behind the conventional method is predicting the target's orientation by the time difference between the laser echo signal and the Hall switch signal. It is set that the arrival moment for the initial Hall switch signal is t_{me0} and that of the second Hall switch signal is t_{me1}. So, $\Delta t_{me} = t_{me1} - t_{me0}$, where t_r represents the arrival time of the laser echo signal. The target orientation angle ϕ is then determined by the following equation:

$$\phi = \phi_0 + \mathrm{mod}[2\pi \frac{t_r - t_{me0}}{\Delta t_{me}}, \frac{2\pi}{k}] \quad (9)$$

where, ϕ_0 is denoted as the initial orientation angle. There are three surfaces of the reflector, so a single rotation of the motor enables three times scanning of the field of view. Therefore, as shown in Figure 10b, the time interval between the two adjacent Hall switch signals can be divided into three scanning regions named (A, B, C) respectively. The target orientation angle is set to -60° on each scanning region's left side and set to 60°on the right side.

Due to spatial limitations, the scanning unit in this study employed a sensorless and brushless motor, which posed challenges in attaining precise control over the motor's rotational speed. So, when the laser echo signal is near the edge of the reflector, the scanning unit may have difficulty accurately identifying the exact scanning region where the target is located. Taking the situation shown in Figure 10b as an example, the scanning unit may randomly judge the target is located in the scanning region A or B. It could potentially result in a significant misinterpretation of the target orientation.

To address the challenges above, this paper introduces a novel magnetic ring to replace the magnetic steel in the conventional approach. As illustrated in Figure 11, the magnetic ring consists of three magnetic poles evenly spaced at 120° intervals, and each pole is positioned to align with the profile face of the reflector. During the operation, the magnetic ring is securely affixed to the laser-receiving reflector, rotating synchronously with the motor.

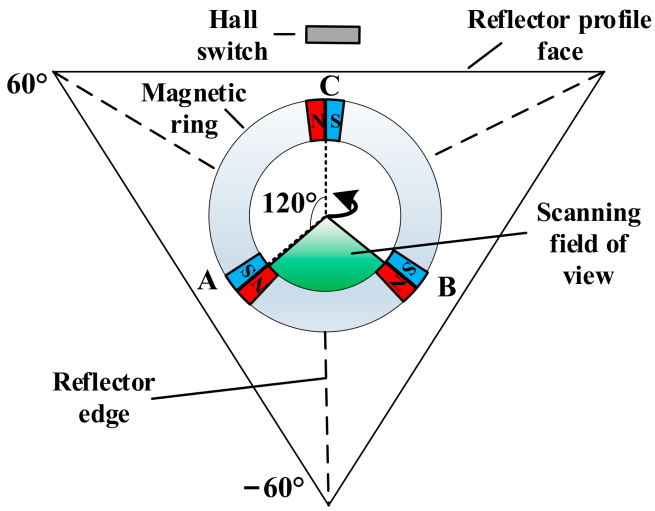

Figure 11. The design of the magnetic ring.

Each Hall switch signal the scanning unit receives indicates the completion of one scanning cycle. At the same time, the reflector completed a transition between scanning regions. In other words, the scanning unit can precisely identify the specific scanning region of the reflector where the target is situated, guided by the Hall switch signal.

In practical detection scenarios, since the volume of the target typically exceeds the size of the scanning unit by far, the target will be detected by multiple pulsed laser beams simultaneously within the field of view, as depicted in Figure 12. However, only a single detection result can be selected. The conventional strategy will immediately send a detection signal, if the target is scanned. It will easily lead to a focused detection on the target's edges.

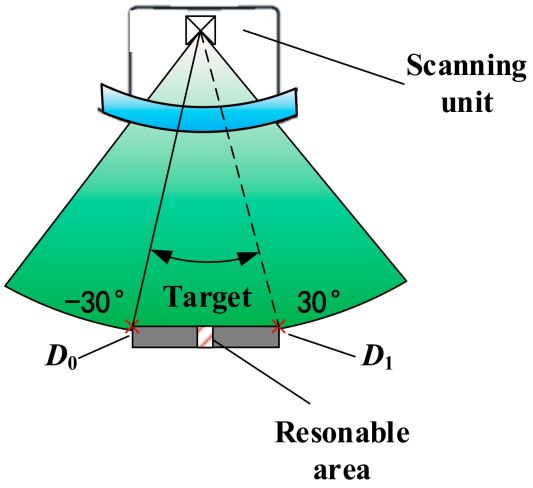

Figure 12. Detonator scanning for large-volume targets.

The detection results should be directed towards the target's reasonable area, commonly identified as the geometric center of the target. Hence, this paper proposes a novel detection strategy as depicted in Figure 12. Within the field of view, the scanning unit records solely the initial orientation (D_0) and the final orientation (D_1) of the target. Finally, the scanning unit outputs the target orientation results (D) for large-volume targets. It can be expressed as below:

$$D = \frac{D_0 + D_1}{2} \tag{10}$$

3.2. FPGA-Based Rapid Detection Method for Target Orientation

The conventional detection result of the target orientation is presented as the output of a counter, which necessitates a complex conversion procedure to transform it into an angular value. This process is not conducive to the implementation of the orientation detection algorithm of large-volume targets, as outlined in Equation (10). Hence, in this study, the scanning field of view was partitioned into eight intervals via binary coding, as illustrated in Figure 13. Each interval encompasses an angular range of 15°.

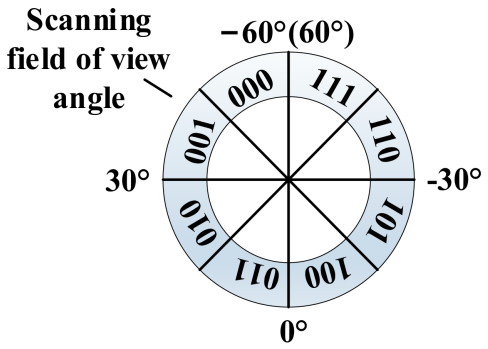

Figure 13. Target orientation encoding correspondence.

Moreover, considering the inherent fluctuations of the motor speed, the count value of Δt_{me} in the Equation (9) exhibits continuous variations. This phenomenon may exert an influence on the results of the target orientation detection. Therefore, in this paper, a finite-state machine was employed to create timestamp and rectify the time interval Δt_{me} between consecutive signals from the Hall switch, as illustrated in Figure 14. Where Eodn represent the nth Eod signal which is captured by the scanning unit.

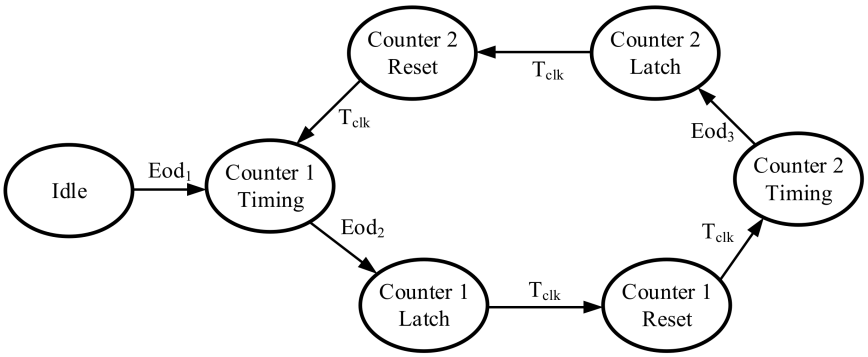

Figure 14. Timing correction by utilizing finite-state machine.

Two times of timing or correction of Δt_{me} are required between three consecutive Hall switch signals, so two counters were employed in the state machine. Counter 1 and Counter 2 operate in a ping-pong mode, upon the arrival of the Eod_1 signal. It also signifies the initiation of the motor. At the same time, the state machine enters a loop, and Counter 1 initiates timing. Upon the arrival of the Eod_2 signal, the timing outcome of Counter 1 will be latched as the initial measurement outcome of Δt_{me}. After a single system clock cycle, T_{clk}, Counter 1 will be reset to zero, and Counter 2 will initiate timing. Upon the arrival of the Eod_3 signal, the timing result of Counter 2 will be latched to rectify Δt_{me}.

Until now, the state machine achieves two corrections to Δt_{me} within one rotation cycle of the motor. In contrast, the traditional orientation detection method depicted in Figure 10 can only perform a single correction for Δt_{me} per rotation cycle. Therefore, the novel magneto–electric detection module proposed in this paper contributes to a 50% reduction in the orientation detection error due to the motor speed fluctuation.

Taking advantage of the parallel processing capabilities in FPGAs, the timing diagram for the program design in this study is depicted in Figure 15. Rec represents the laser echo signal, and Hit denotes the trigger signal, which is activated only upon the first reception of the Rec signal. Hall signifies the Hall switch signal. Clk_2 corresponds to the two-division clock of Δt_{me}, and Clk_4 (Clk_8) denotes the four (eight) division clock of Δt_{me}. D0_reg refers to the register encoding the target's initial orientation, and D1_reg designates the register encoding the target's termination orientation as mentioned in Equation (10). The Eod signal serves as an end-of-detection flag used to lock the measurement result. The Rst signal functions as a reset signal to pull the Hit signal low and clear the D_reg signal in preparation for the subsequent cycle.

To implement the encoding method depicted in Figure 13 on FPGA, this paper divides Δt_{me} into 2, 4, and 8 divisions to generate three split-frequency clocks. Based on the level distribution of these three split-frequency clocks, Δt_{me} can be segmented into eight intervals labeled Q1 to Q8, as depicted in Figure 15. Whenever the Rec signal is received, the scanning unit can effectively encode the target's orientation based on its position within Q1 to Q8.

As depicted in Figure 15, the main function of the target initial orientation code hosting circuit is to capture and preserve the orientation code upon detecting the first Rec signal within the Δt_{me} interval. Subsequent Rec signals do not change the value of D0_reg. The circuit design for this module is illustrated in Figure 16a. It employed the rising edge of the asynchronous trigger signal, Hit, for split-frequency clock sampling. To prevent potential metastability, the sampled results are repetitively latched using the system clock Sys_Clk. This process facilitates the conversion of D0_reg into a synchronous signal for output.

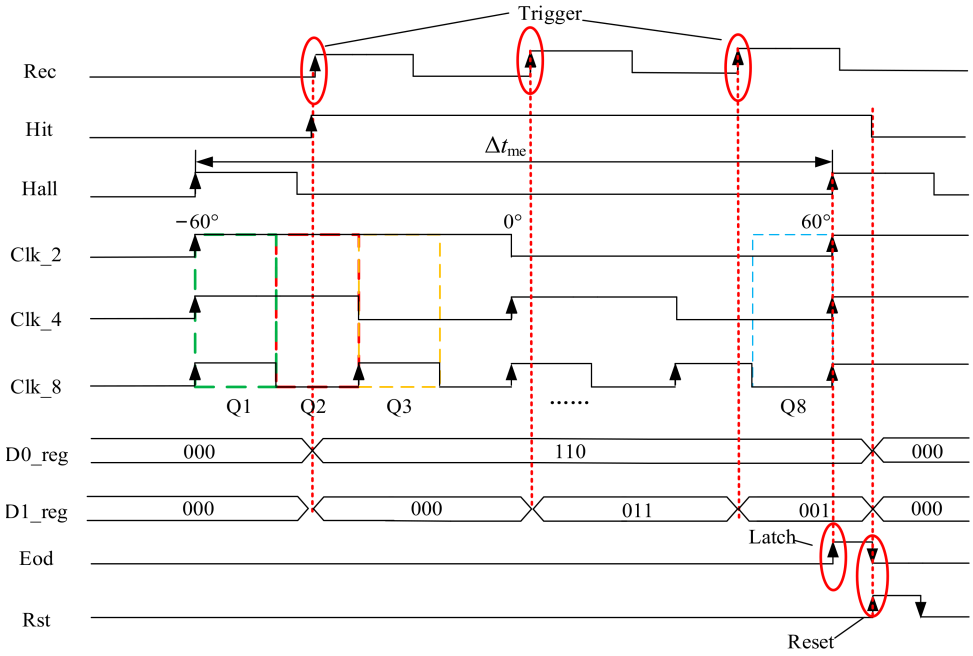

Figure 15. FPGA program timing.

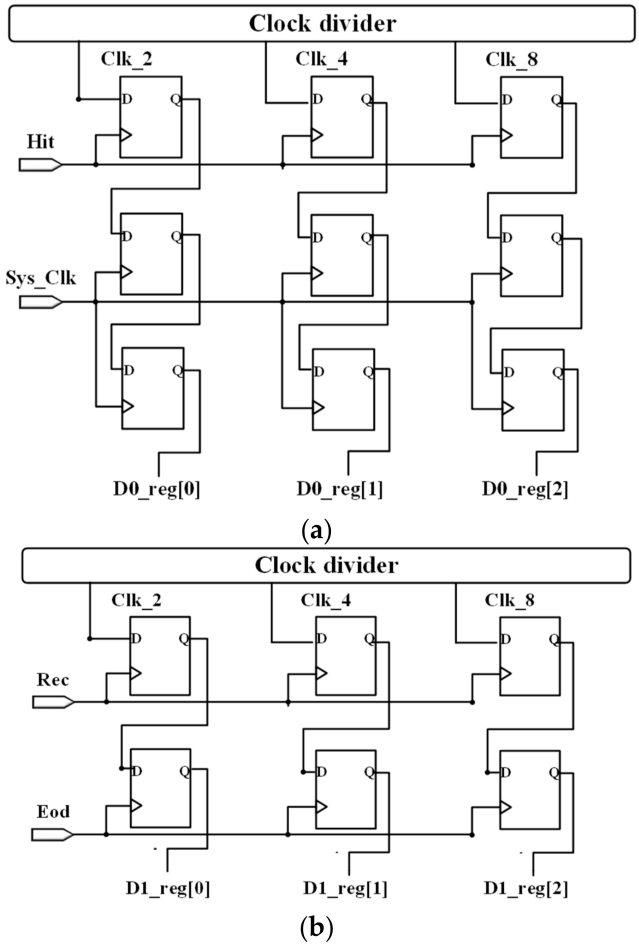

Figure 16. Initial and termination orientation coding register circuit of targets: (**a**) Hosting circuit of initial orientation codes of targets; (**b**) Hosting circuit of termination orientation code of targets.

In Figure 16b, the register for encoding the target termination orientation, D1_reg, is continuously updated in response to each Rec signal. Still, the final result is latched only upon completion of the entire scanning, marked by the arrival of the Eod signal.

By utilizing the encoded results D0_reg and D1_reg along with Equation (10), the specific outcomes for target orientation detection within the field of view range can be promptly obtained, with an output delay of just one system clock cycle.

4. Experiment Results and Analysis

4.1. Air Test

The Figure 17 shows the prototype and the experiment scenario of the scanning unit. The stable power supply was used to drive the laser receiving circuit, the Hall switch, and the brushless motor. The laser served as the pulsed light source, while the oscilloscope was utilized to monitor the Hall switch signal.

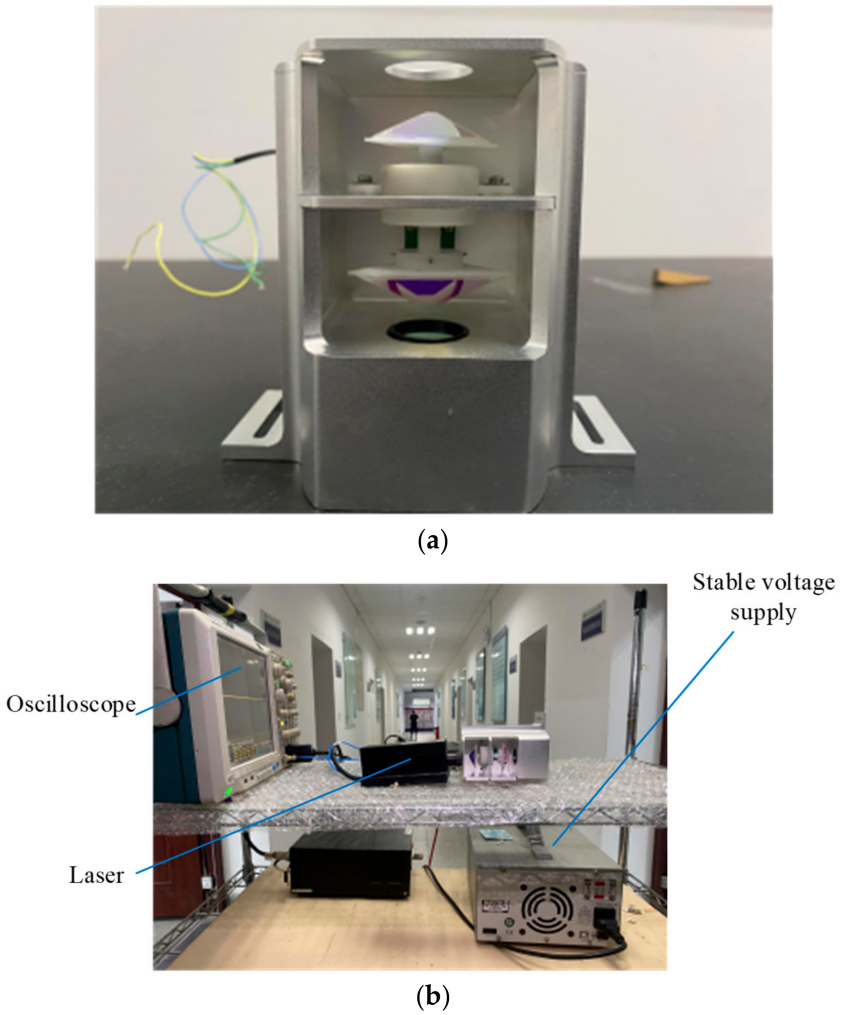

Figure 17. Prototype and experiment scenario: (**a**) Prototype of the scanning unit; (**b**) Experimental scenario.

As depicted in Figure 18, when the pulse laser and brushless motor are activated, the scanning unit follows a straight-line trajectory within the scanning field of view.

The length of the scanning trajectory was measured by placing the target plate at distances of 0.2–0.4 m from the prototype, respectively. The measurement results are presented in Table 2, and the field of view is approximately 113°, consistent with the simulation calculations in the Section 2.

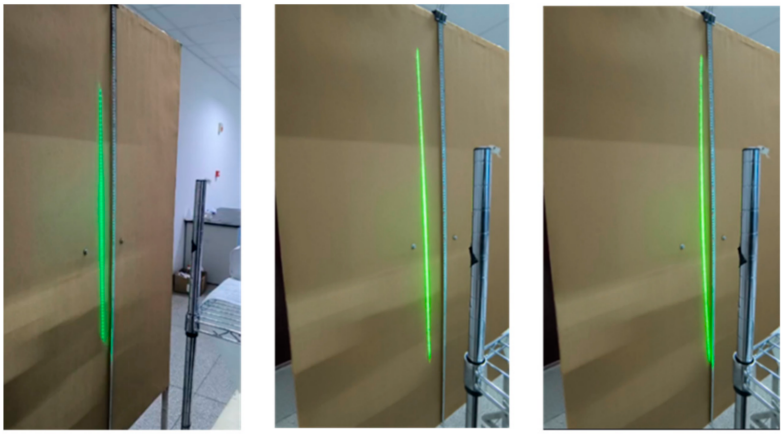

Figure 18. Laser scanning trajectory in the experiment. (**a**) Target plate prototype spacing 0.2 m; (**b**) Target plate prototype spacing 0.3 m; (**c**) Target plate prototype spacing 0.4 m.

Table 2. Prototype field of view measurement results.

Spacing of the Target Plate Prototype (m)	Scanning Track Length (m)	Field of View Angle (°)
0.20	0.61	113.6
0.30	0.91	113.2
0.40	1.22	113.4

Simultaneously, the results of an oscilloscope monitoring the Hall switch signal are shown in Figure 19. The scanning unit receives consistent signals from the Hall switch while the motor is rotating. Furthermore, for the scanning unit, every two consecutive Hall switch signals correspond to completing a scanning cycle within the field of view.

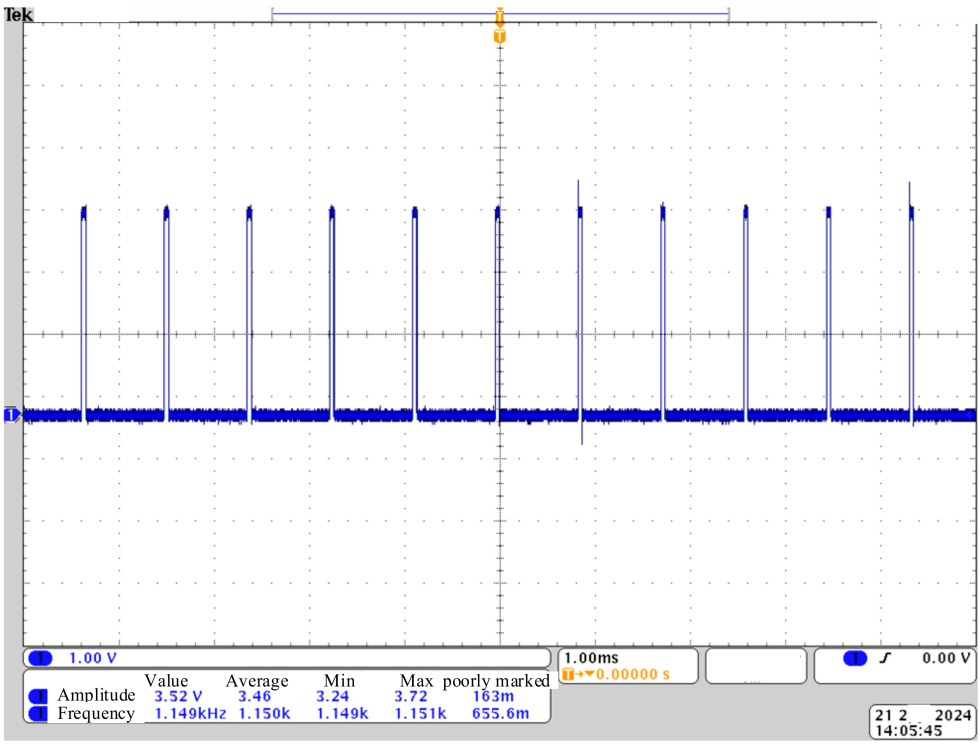

Figure 19. Hall switch signal diagram.

The laser echo signal "Rec" and the Hall switch signal "Hall" received by the scanning unit are collected into the FPGA. As illustrated in Figure 20, each Hall switch signal represents the completion of edge switching by the reflector. The system clock (sys_clk) was employed to sample the Hall signal at the rising edge, referred to as the "Eod" signal. This enables the scanning unit to accurately identify the reflector's edge (as shown in Figure 11) within a nanosecond delay. So, the scanning unit can precisely identify the specific scanning region of the reflector where the target is situated.

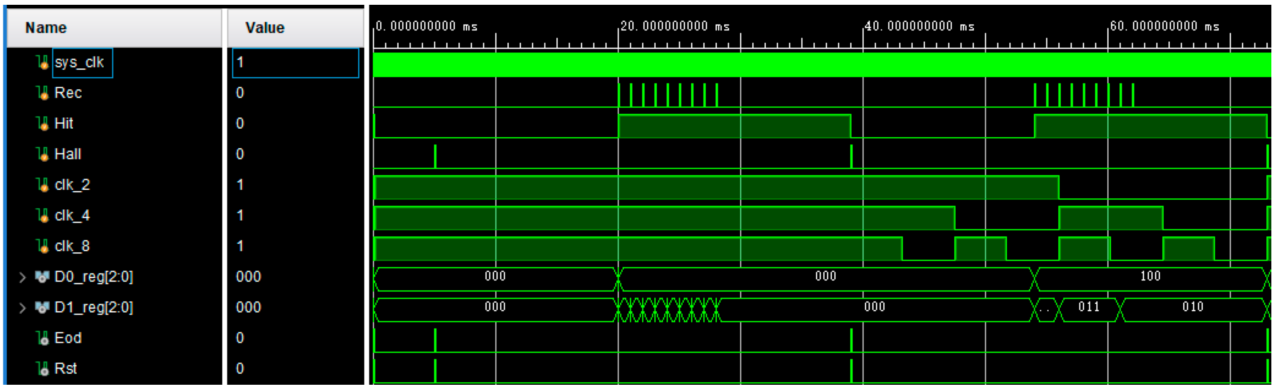

Figure 20. FPGA implementation of the orientation detection program.

Furthermore, the scanning unit does not provide valid orientation angle measurements upon receiving the first two Hall signals. It is because the timing of Δt_{me} has not yet been completed at this stage, which prevents the generation of the correct split-frequency clocks. However, when the third Hall signal is received, the initial timing result of Δt_{me} can be utilized to generate the split-frequency clocks, Clk2~Clk8. Simultaneously, one program cycle is finalized upon completion of the second timing of Δt_{me} and the subsequent correction. Then, the scanning unit can achieve the following recognition of the target orientation after a single system clock cycle (20 ns) whenever it receives a Hall signal.

When the scanning unit receive multiple laser echo signals within the scanning field of view, the program will focus on identifying the initial and termination-orientational encodings of the target. Then, by using Equation (10), the scanning unit can identify the weak sections for a large-volume target.

As illustrated in Figure 20, the initial and termination-orientational encoding of the target are 100 and 010. They represent target orientation angles of $-15°$ and $30°$, respectively. So, the final output of the scanning unit is $7.5°$, according to Equation (10).

4.2. Pool Test

We conducted the target echo signal acquisition tests in pool environments to verify further the capability of scanning. Figure 21 shows the experimental scenario for the pool test. Unlike the air experiments, this experiment simulates the challenges that the laser may face as it passes through the glass and enters the aqueous medium.

The laser first passes through the glass to form a beam in the water, which is reflected to the target surface and then returned to the air to be received by the scanning unit. Move the target to 1 m, 8 m, and 10 m from the scanning unit, and get the target echo signal as shown below. Therefore, pool tests verify that the scanning unit proposed in this paper can realize reliable scanning through glass and water.

As shown in Figure 22, unlike detection in air, a backscattered echo peak is received before the target echo peak due to water's strong attenuation and scattering effect on the laser. As the detection distance increases, the two echo peaks gradually separate, and the amplitude of the target echo peak decreases.

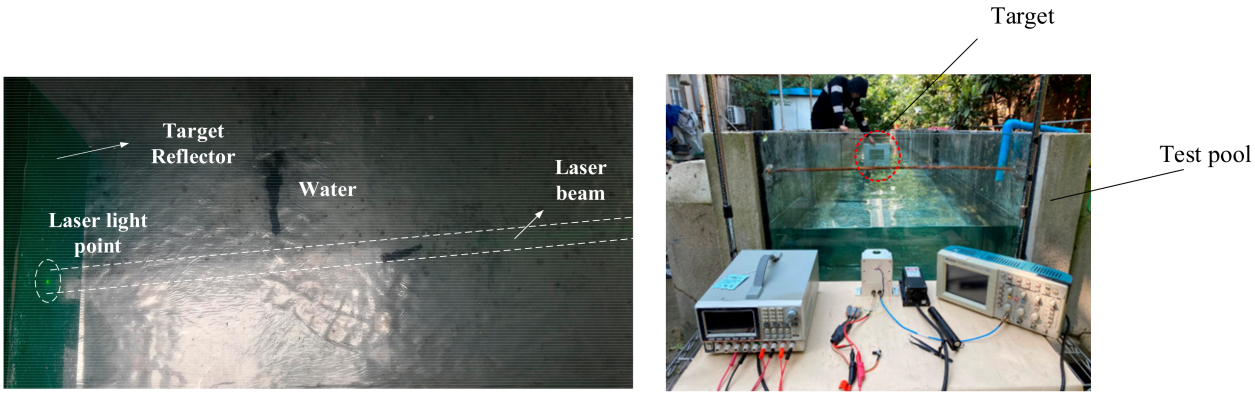

Figure 21. The diagram of the pool test.

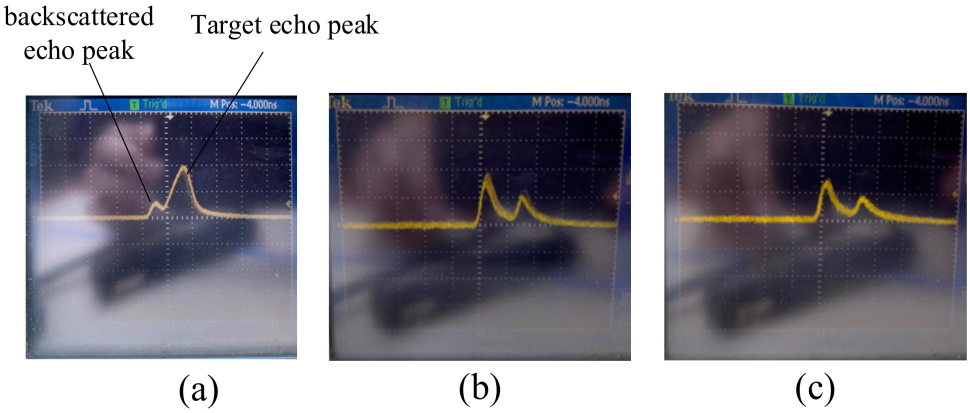

Figure 22. Echo signals received by targets at different distances: (**a**) 1 m from the scanning unit; (**b**) 8 m from the scanning unit; (**c**) 10 m from the scanning unit.

5. Discussion

In the test section of Chapter 4, the scanning unit's abilities to scan in the air and detect a target's orientation were verified, respectively. Due to space constraints, the pool test verified that the scanning unit was capable of reliably scanning a target, even when faced with the challenges of scanning through enclosures and then through an aqueous medium. However, in the pool test, we noticed that there are two peaks in the echo signal; the first one is the backscattered echo peak, and the other one is the target echo peak. The amplitude of the target echo peak is larger than that of the backscattered echo peak at close range, and the amplitude of the target echo peak gradually decreases with the increase of the detection distance. And it is even lower than the amplitude of the backscattering echo peak. Therefore, its presence will seriously reduce the underwater LiDAR's accuracy. Thus, when the scanning unit is applied to underwater laser detection, it needs to be equipped with a signal processing system to filter out the backscattered echo peak to improve the ranging accuracy.

6. Conclusions

This paper proposes a scanning unit for LiDAR based on pyramidal-shaped reflectors, which enables efficient laser scanning and fast target orientation detection. It suits the four-quadrant transceiver scheme proposed in this paper and holds reference values for other underwater LiDAR. The main conclusions are as follows:

(1) A laser scanning trajectory model was established based on the characteristics of reflector, and a multi-parameter optimization design was carried out. The results indicate that when the cone angle θ of the reflector is not equal to 45°, the scanning trajectory will take the shape of a parabola. It can cause the actual field of view to be much smaller than the theoretical field of view. Furthermore, compared to the traditional single-beam

synchronized scanning schemes, the scanning unit can complete three scanning cycles within the field of view during one rotation cycle, tripling the scanning efficiency.

(2) When the laser echo signal is close to the edge of the reflector, the conventional orientation detection method may lead to a significant misinterpretation of the target orientation. So, this paper proposed a new magneto–electric detection module that consists of a Hall switch and a novel magnetic ring. It can enable the identification of reflector's edges with nanosecond delay (20 ns). Furthermore, since the volume of the target typically exceeds the size of the scanning unit by far, the conventional strategy will only lead to a focused detection on the target's edges. To optimize the damage effects, a new detection strategy is explicitly designed to identify the reasonable parts for large-volume targets.

(3) An FPGA-based rapid target orientation identification method was proposed in this paper. It integrates a real-time timing and correction approach for motor speed using finite state machines and a rapid target orientation coding method based on a split-frequency clock sampling. The experimental results confirm that the speed measurement results of the brushless motor can be corrected twice within a single cycle of motor rotation. Furthermore, the new target orientation identification method proposed in this paper effectively measure the target's initial and termination orientation encoding, yielding target orientation detection results immediately after the scanning process with an output delay of only 20 ns.

The future work will focus on constructing the entire system and developing signal-processing algorithms to test underwater LiDARs comprehensively.

Author Contributions: Methodology, B.Z., Y.T., J.Q. and H.Z.; Software, Z.C. and Y.T.; Writing—original draft, G.X. All authors have read and agreed to the published version of the manuscript.

Funding: This work is supported by the National Natural Science Foundation of China, grant number 52201399; the China Postdoctoral Science Foundation, grant number 2021M701713; the Jiangsu Funding Program for Excellent Postdoctoral Talent, grant number 20220ZB245; Postgraduate Research & Practice Innovation Program of Jiangsu Province, grant number KYCX23_0511.

Data Availability Statement: The main innovative content of this article is circuit design, and there is no valuable data to share.

Acknowledgments: The authors would like to thank the peer reviewers and editors for their hard work and constructive feedback, which will make a significant contribution to improving the paper.

Conflicts of Interest: The authors declare no conflicts of interest.

References

1. Zheng, Z.; Zha, B.; Zhou, Y.; Huang, J.; Xuchen, Y.; Zhang, H. Single-Stage Adaptive Multi-Scale Point Cloud Noise Filtering Algorithm Based on Feature Information. *Remote Sens.* **2022**, *14*, 367. [CrossRef]
2. Zhang, W.; Qi, J.; Wan, P.; Wang, H.; Xie, D.; Wang, X.; Yan, G. An Easy-to-Use Airborne LiDAR Data Filtering Method Based on Cloth Simulation. *Remote Sens.* **2016**, *8*, 501. [CrossRef]
3. Cai, Z.; Liu, X.; Peng, X.; Yin, Y.; Li, A.; Wu, J.; Gao, B.Z. Structured light field 3D imaging. *Opt. Express* **2016**, *24*, 20324–20334. [CrossRef] [PubMed]
4. Yuan, H.L.; Zhang, H.; Zha, B.T.; Ding, L.B. Trajectory correction and position error analysis of underwater laser scanning. *Opt. Laser Technol.* **2022**, *153*, 108136. [CrossRef]
5. Li, Z.-P.; Ye, J.-T.; Huang, X.; Jiang, P.-Y.; Cao, Y.; Hong, Y.; Yu, C.; Zhang, J.; Zhang, Q.; Peng, C.-Z.; et al. Single-photon imaging over 200 km. *Optica* **2021**, *8*, 344–349. [CrossRef]
6. Maccarone, A.; McCarthy, A.; Ren, X.; Warburton, R.E.; Wallace, A.M.; Moffat, J.; Petillot, Y.; Buller, G.S. Underwater depth imaging using time-correlated single-photon counting. *Opt. Express* **2015**, *23*, 33911–33926. [CrossRef] [PubMed]
7. Pokorny, P. One-mirror and two-mirror three-dimensional optical scanners position and accuracy of laser beam spot. *Appl. Optics* **2014**, *53*, 2730–2740. [CrossRef] [PubMed]
8. Keskin, A.; Baykal, Y. Scintillation and BER analysis of cosine and cosine-hyperbolic-Gaussian beams in turbulent ocean. *Appl. Opt.* **2021**, *60*, 7054–7063. [CrossRef] [PubMed]
9. Maccarone, A.; Drummond, K.; McCarthy, A.; Steinlehner, U.K.; Tachella, J.; Garcia, D.A.; Pawlikowska, A.; Lamb, R.A.; Henderson, R.K.; McLaughlin, S.; et al. Submerged single-photon LiDAR imaging sensor used for real-time 3D scene reconstruction in scattering underwater environments. *Opt. Express* **2023**, *31*, 16690–16708. [CrossRef]

10. Shangguan, M.; Weng, Z.; Lin, Z.; Lee, Z.; Yang, Z.; Sun, J.; Wu, T.; Zhang, Y.; Wen, C. Day and night continuous high-resolution shallow-water depth detection with single-photon underwater lidar. *Opt. Express* **2023**, *31*, 43950–43962. [CrossRef]
11. Macdonald, I.R.; Chu, J.S.; Reilly, F.F.; Blincow, M.; Olivier, D. Deep-ocean use of the SM2000 laser line scan-ner on submarine NR-1 demonstrates system potential for industry and basic science. In Challenges of Our Changing Global Environment, Proceedings of the OCEANS '95 MTS/IEEE, San Diego, CA, USA, 9–12 October 1995; IEEE: Piscataway, NJ, USA, 1995; Volume 1, pp. 555–565.
12. Fournier, G.R.; Bonnier, D.; Forand, J.L.; Pace, P.W. LUCIE ROV mounted laser imaging system. In Proceedings of the Ocean Optics XI. SPIE, San Diego, CA, USA, 20–22 July 1992; Volume 1750, pp. 443–452.
13. Steinvall, O.; Andersson, P.; Elmquist, M. *Image Quality for Range-Gated Systems during Different Ranges Atmospheric Conditions*; International Society for Optics and Photonics: Bellingham, WA, USA, 2006; p. 639607.
14. Fuchse, T. Conceptual Design of the CZMIL Data Acquisition System (DAS): Integrating a New Bathymetric LiDAR with a Commercial Spectrometer and Metric Camera for Coastal Mapping Applications. In Proceedings of the SPIE7695, Algorithms and Technologies for Multispectral, Hyperspectral, and Ultraspectral Imagery XVI, Orlando, FL, USA, 5–9 April 2010; SPIE: Bellingham, WA, USA, 2010.
15. Zeng, X.; Xia, M.; Cheng, Z.; Li, L.; Chen, J.; Du, P.; Yang, K. A small-size pulsed lidar designed for obstacles detection in natural underwater environment. In *AOPC 2015: Optical and Optoelectronic Sensing and Imaging Technology*; SPIE: Bellingham, WA, USA, 2015; Volume 9674, pp. 381–386.
16. Maccarone, A.; Della Rocca, F.M.; McCarthy, A.; Henderson, R.; Buller, G.S. Three-dimensional imaging of stationary and moving targets in turbid underwater environments using a single-photon detector array. *Opt. Express* **2019**, *27*, 28437–28456. [CrossRef] [PubMed]
17. Zha, B.T.; Yuan, H.L.; Ma, S.J.; Chen, G.S. Influence of single-beam expanding scanning laser circumferential detection system parameters on detection capability. *Acta Phys. Sin.* **2019**, *68*, 79–88. [CrossRef]
18. Tan, Y.Y.; Zhang, H.; Zha, B.T. Simulation of underwater LiDAR echo on the basis of bidirectional reflectance distribution function. *Acta Photonica Sin.* **2016**, *45*, 59–64.
19. Chen, S.S.; Zhang, H.; Xu, X.B. Echo characteristic of planar target in pulsed LiDAR detection. *Acta Armamentarii* **2018**, *39*, 1095–1102.
20. Gan, L.; Zhang, H. Underwater laser autonomous scanning short-range orientation detection method on the basis of fluid-driven. *Chin. J. Lasers* **2019**, *46*, 0304004.
21. Cheng, Z.; Yang, K.; Han, J.; Zhou, Y.; Sun, L.; Li, W.; Xia, M. Improved time-of-flight range acquisition technique in underwater LiDAR experiments. *Appl. Opt.* **2015**, *54*, 5715–5725. [CrossRef] [PubMed]
22. Yuan, H.; Zha, B.; Zhang, H. Parameter Optimization of Geometrically Truncated Ranging LiDAR System. *Infrared Laser Eng.* **2018**, *47*, 97–102.
23. Tan, Y.Y.; Zhang, H.; Zha, B.T. Underwater single beam circumferentially scanning detection system using range-gated receiver and adaptive filter. *J. Mod. Opt.* **2017**, *64*, 1648–1656. [CrossRef]
24. Zhong, K.; Su, W.; Peng, B.; Huang, S. Design of 4f emission optical system for underwater laser peripheral scanning. *Infrared Laser Eng.* **2021**, *50*, 199–210.
25. Xu, X.; Zhang, L.; Yang, J.; Cao, C.; Wang, W.; Ran, Y.; Tan, Z.; Luo, M. A Review of Multi-Sensor Fusion SLAM Systems Based on 3D LIDAR. *Remote Sens.* **2022**, *14*, 2835. [CrossRef]
26. Xu, G.; Zha, B.; Yuan, H.; Zheng, Z.; Zhang, H. Underwater four-quadrant dual-beam circumferential scanning laser fuze using nonlinear adaptive backscatter filter based on pauseable SAF-LMS algorithm. *Def. Technol.* **2023**, in press. [CrossRef]
27. Xu, G.B.; Zha, B.T.; Zheng, Z.; Zhang, H. Design and modeling of small-opening cascade sync-scanning underwater LiDARs. *Acta Armamentarii* **2022**, *43*, 3162–3171.
28. Gan, L.; Wang, K.; Xu, Z.; Zhang, N.; Zhang, H. Influence of periodically scanning magnetic signal characteristics on the statistical distribution of laser-magnetic composite azimuth detection. *Chin. J. Sci. Instrum.* **2022**, *43*, 235–243. [CrossRef]
29. Xu, G.; Zha, B.; Xia, T.; Zheng, Z.; Zhang, H. A high-throughput vernier time-to-digital converter on FPGAs with improved resolution using a bi-time interpolation scheme. *Appl. Sci.* **2022**, *12*, 7674. [CrossRef]